Carbon 196 (2022) 972–978

Contents lists available at ScienceDirect

Carbon

journal homepage: www.elsevier.com/locate/carbon

Formation of Q-carbon with wafer scale integration

Parand R. Riley [a], Pratik Joshi [a], Nayna Khosla [a], Roger J. Narayan [b,*], Jagdish Narayan [a]

[a] Department of Materials Science and Engineering, Centennial Campus, North Carolina State University, Raleigh, NC, 27695-7907, USA
[b] Joint Department of Biomedical Engineering, Centennial Campus, North Carolina State University, Raleigh, NC, 27695-7115, USA

ARTICLE INFO

Keywords:
Q-carbon
Scale-up production
Low-energy ion bombardment
Radio frequency plasma-enhanced chemical vapor deposition

ABSTRACT

We describe the formation of highly uniform Quenched-carbon (Q-carbon) layers by plasma-enhanced chemical vapor deposition (PECVD) followed by low-energy Ar^+ ion bombardment to achieve wafer-scale integration of Q-carbon films. After PECVD, 9 nm and 20 nm thick silicon-doped diamond-like carbon (Si-DLC) films showed complete conversion into Q-carbon using 250eV Ar^+ ions via negative biasing. However, this conversion was only partial for 30 nm thick films. Detailed EELS, XPS, Raman, and EDS studies were carried out to confirm the formation of Q-carbon by this method. We discuss the mechanism of Q-carbon formation as a result of low-energy ion bombardment during PECVD of thin films. These ions during negative biasing are energetic enough to create Frenkel defects, which support the conversion of the three-fold coordinated sp^2 carbon units in as-deposited carbon into sp^3 bonded five-atom tetrahedron units in Q-carbon. This process enhances the atomic number density and fraction of sp^3 bonded carbon. These diamond tetrahedra are randomly packed and provide easy nucleation sites for diamond. If the underlying substrate can provide an epitaxial template for diamond growth via domain matching epitaxy, then wafer-scale growth of diamond epitaxial films can be achieved for wafer-scale integration and next-generation novel device manufacturing from diamond-related materials.

1. Introduction

Quenched-carbon (Q-carbon) is a new allotrope of carbon with a unique structure and many extraordinary properties. Q-carbon consists of randomly packed tetrahedra with four-fold sp^3-hybridized carbon (>75–80%) and the rest three-fold sp^2-hybridized carbon at the interface [1]. This allotrope has a higher number density of covalently bonded carbon atoms than diamond; therefore, it is harder than diamond because hardness is shown to scale approximately with the number density of atoms [2]. The diamond crystal lattice (DCL) has the highest number density of covalently bonded carbon atoms (1.77×10^{23} cm^{-3}), which provides it with ultra-high hardness properties. However, DCL has the lowest atomic packing fraction (APF) of 34% (compared to 74% for the close-packed FCC and HCP lattices). This low APF attracted us to make efforts to enhance the number density of atoms and create new covalently bonded materials. Upon a closer examination of the diamond unit cell, it was found that the diamond cubic unit cell consists of two types of tetrahedra, one with central atoms (D1) and the other with a missing central atom (D2). The unit cell consists of four D1 and four D2, which alternate to create the DCL, with 8 atoms per unit cell. It occurred to us that by putting together D1 only, we can gain 4 atoms and increase the number of atoms to 12 atoms per unit cell, thereby increasing the APF to 51%; this value is still lower than the APF for the simple cubic structure (54%). This unit cell with 12 atoms has the CaF_2 structure; however, this covalently bonded carbon unit cell cannot be repeated as the face atoms already have four covalent bonds. However, D1 tetrahedra can be packed randomly and lead to a 60% higher number density of atoms with 80% packing efficiency of D1. This is the essence of the discovery of Q-carbon, in which D1 are formed in a metallic undercooled carbon melt, quenched rapidly, and packed to create a new structure with many extraordinary properties [3,4].

The Q-carbon is an ideal ultrahard coating since it is harder, tougher, and more adherent than diamond. Undoped Q-carbon exhibits robust room-temperature ferromagnetism [1]. Upon doping with B, Q-carbon forms amorphous polymorphs with distinct record superconducting transition temperatures [3,5]. This process is consistent with our basic understanding of the intimate relationship between hardness and superconductivity through Debye frequency and spring constant (stiffness). In addition, Q-carbon provides easy nucleation sites for diamond growth by conventional HFCVD, PECVD, and MWCVD, all of which require seeding for diamond growth. If the underlying substrate can provide an epitaxial template via domain matching epitaxy, then it is

* Corresponding author.
E-mail address: rjnaraya@ncsu.edu (R.J. Narayan).

https://doi.org/10.1016/j.carbon.2022.06.003
Received 31 March 2022; Received in revised form 20 May 2022; Accepted 2 June 2022
Available online 6 June 2022

possible to achieve wafer-scale epitaxial growth of diamond films [6].

Until now, Q-carbon has been produced by laser irradiation of diamond-like carbon (DLC) films using a nanosecond pulsed excimer laser [7]. During the pulsed laser annealing (PLA) method, the DLC film experiences a fast undercooling and a first-order phase transformation from liquid to solid, which culminates in the formation of Q-carbon. The Gibbs free energy (ΔG_T) is given by $\Delta G_T = -\Delta H_m . \Delta T_u/T_m$, where ΔT_u is the undercooling, ΔH_m is the enthalpy of melting, and T_m is the melting temperature. Thus, the driving force for Q-carbon formation is provided by the undercooling ΔT_u. We have shown that a high undercooling (>1000 K) and fast quenching are necessary for this transformation [7,8].

Past efforts involving the deposition of diamond using plasma-enhanced chemical vapor deposition (PECVD) have shown that by applying negative bias, an amorphous layer of carbon is generated; the diamond nucleation increases on the amorphous carbon layer. The carbon layer formed during the biasing is responsible for the greater diamond nucleation density. Yugo et al. described an improvement in diamond nucleation by applying negative bias during the PECVD process [9]. Stoner et al. utilized negative biasing during bias-enhanced microwave PECVD for diamond synthesis on a silicon substrate. They described the formation of an amorphous layer of silicon carbide with a thin layer of amorphous carbon on top due to biasing [10]. They noted that the amorphous carbon layer plays an important role in the improvement of diamond nucleation. Kim et al. also detected the formation of a carbon layer on the top surface of bias-treated substrates during the bias enhanced nucleation (BEN) process for the growth of diamond [11]. Later, when the BEN process was used by Schreck et al. for diamond nucleation, the emergence of some bright domains during the BEN process was an interesting observation [12]. The diamond nucleation and growth were significantly higher and epitaxial inside the domains compared to outside the domains. They reported that the bright domains were highly stable; however, they did not provide a detailed structural understanding of the domains. Liao et al. revealed that the main mechanism for the enhancement in diamond nucleation during the BEN procedure is ion bombardment [13]. In another study, Schreck et al. suggested that during the ion bombardment in the microwave PECVD process, the ions promote the formation and lateral growth of the domains with a lateral growth velocity of 1.67 nm/s [14]. However, such a growth rate is not possible without excessive displacement damage. Recently, Narayan et al. proposed mechanisms to explain the structure of the amorphous carbon layer produced by negative biasing [15]. They noted that since the domains are highly rich in sp^3 content with some diamond components [13–15], the structure of the domains is very similar to the Q-carbon structure. They also provided the mechanisms for the formation of Q-carbon domains under low-energy ion bombardment in the solid state. Based on this theory, the energy of the ions during ion bombardment is high enough for the formation of Frenkel pairs per ion. The Frenkel pairs consequently convert the sp^2 carbon bonds into sp^3 carbon bonds. The energy is adequate to stabilize and produce compact sp^3 diamond tetrahedra units that are needed for the Q-carbon structure.

In the present work, the formation of silicon-doped Q-carbon (Si-Q-carbon) by low-energy ion bombardment in a PECVD chamber using appropriate values of negative bias was demonstrated. In this process, the CH_3^+ ion bombardment assisted with the formation of sp^3 carbon bonds. Postprocessing of the surface of Si-Q-carbon by argon ion bombardment was performed to obtain a first-order phase transformation of sp^2 bonds into sp^3 bonds for Q-carbon formation. Our analysis shows the formation of silicon-doped Q-carbon with a high content of sp^3 C–C bonds (up to 86%). We have examined the changes in the structure and the sp^3 content of the Si-Q-carbon films with an increasing duration of CH_3^+ ion bombardment during the deposition process. The mechanism of Q-carbon formation using low-energy ion bombardment is discussed in detail. This method provides the capability of Q-carbon production at a large scale (up to 12" wafer) with controlled thickness. The ability to produce continuous Q-carbon at a large scale is important for industrial applications. Therefore, this method is suitable for Q-carbon and diamond coatings for applications such as protective coatings and diamond-based electronic devices.

2. Materials and methods

2.1. Si-Q-carbon deposition by PECVD

The silicon (100) substrates 6" diameter were cleaned by ultrasonication in an acetone bath for 5 min and then in methanol bath for 5 min. The substrates were immediately loaded inside the chamber of the deposition system. The deposition system utilized in this work is a Radio Frequency Plasma-Enhanced Chemical Vapor Deposition (RF-PECVD) system in the Nanofabrication Facility (NNF) at North Carolina State University (NCSU). The PECVD system is a custom-designed system that generates plasma in a capacitively coupled mode. The stainless-steel chamber of the system has a cylindrical shape and is custom manufactured for deposition on large-size substrates. In the capacitively coupled mode, plasma is generated between a driving electrode that is connected to a radio frequency power supply and a counter electrode. In this system, the driving electrode with a diameter of 12 inches is seated on the bottom plate of the chamber and also serves as the substrate holder. Thus wafers up to 12" diameter can be used for Q-carbon deposition. The driving electrode is connected to an RF power supply (RFX-600, Advanced Energy, Denver, CO, USA) with a 13.56 MHz frequency; it is electrically insulated from the rest of the chamber, which serves as the counter electrode. The counter electrode is grounded; the chamber is equipped with a water-cooling system. The pumping system provides a base pressure of approximately 2×10^{-8} Torr. The process gases flowed inside the chamber from above through a showerhead distribution ring. The deposition procedure was comprised of loading, plasma cleaning, plasma deposition, postprocessing, and unloading steps. After a pump-down for at least 3 h and attainment of the base pressure, a plasma cleaning procedure was carried out for 10 min using argon gas with a mass flow rate of 90 SCCM. The deposition step was carried out using 1.6 SCCM of tetramethylsilane (TMS) and 90 SCCM of argon for 3 min, 4.5 min, and 6 min to obtain the 9 nm, 20 nm, and 35 nm samples, respectively. During the deposition step, the peak-to-peak voltage (V_{pp}) was maintained at 300 ± 10 V with an RF power of 83 ± 10 W and a DC bias of −150 ± 10 V. The postprocessing plasma treatment was performed by 90 SCCM argon gas for 5 min with a V_{pp} of 500 ± 10 V, an RF power of 160 ± 10 W, and a DC bias of 250 ± 10 V. During all of the procedures, the total pressure was kept at 50 mTorr by a Baratron gauge (MKS, Andover, MA, USA).

2.2. Si-Q-carbon characterization

The thickness of the samples was estimated by the contact profilometry method through the step-height measurement technique using a Dektak D150 (Veeco, Plainview, NY) with a tip size of 12.5 μm in radius. The thickness of the samples was evaluated using cross-section high-resolution TEM imaging from prepared cross-sectional samples. Raman characterization was conducted using an alpha300 M confocal microscope system (WITec, Ulm, Germany); the instrument was equipped with a 532 nm solid-state green light laser and a UHTS 300 spectrometer. The laser spot size was ~2 μm in diameter; the grating size was 600 I/mm. The Raman spectra were calibrated using the standard characteristic peak of silicon (520.6 cm^{-1}). The cross-sectional samples were prepared using a Focused Ion Beam (FIB) technique (Quanta 3D FEG, FEI, Hillsboro, OR, USA). The cross-sectional images, the energy-dispersive X-ray analysis (EDS) data, and electron energy-loss spectroscopy (EELS) data were obtained with a high-resolution transmission electron microscope (S/TEM, Talos-F200 microscope, Hillsboro, OR, USA) with an 'XFEG' Schottky field emission electron gun source operating at 200 keV. The EELS signals were acquired using a collection

semi-angle of 5 mrad and a dispersion of 0.25 eV/channel. X-ray photoelectron spectroscopy (XPS) data were acquired using an Axis Ultra XPS system (Kratos Analytical, Spring Valley, NY, USA); the instrument contains monochromated aluminum Kα (1.487 keV) as the X-ray excitation source. For the survey scan, a pass energy of 160 eV was utilized; for the region scan, a pass energy of 20 eV was utilized. All of the data were calibrated to the C–C peak at 284.8 eV.

3. Results and discussion

3.1. The silicon-doped Q-carbon formation

The thickness of the three sets of samples was measured to be 9 ± 0.5 nm, 20 ± 0.5 nm, and 35 ± 0.5 nm by using the contact profilometry method. Raman analysis, which provides information about the vibrational modes and bonding of the samples, is shown in Fig. 1. The Gaussian distribution was utilized for the deconvolution of the peaks. All of the signals can be deconvoluted into two peaks. The fitted peak at around 1320 cm^{-1}, which is known as the D peak, is assigned to the breathing mode of the sp^2 bonds due to the presence of defects in the structure [16]. The second fitted peak at around 1485 cm^{-1} is the G peak and is ascribed to the stretching of the sp^2-bonds present in the rings or chains [17,18]. For carbon structures that are not doped with silicon, the D and G peaks are typically observed at higher wavenumber values [19]. With the incorporation of silicon atoms in the lattice of the carbon structures, a downshift in the D and G peak positions was observed [20–23]. Since silicon can only form fourfold-coordinated links with carbon atoms, it cannot form the threefold-coordinated configuration. Therefore, no π-bond will form with silicon atoms, and the ratio of sp^3/sp^2 in the structure increases. This process shrinks the size of the sp^2 domains in the structure. The increase in the sp^3 content results in the reduction of the internal residual compressive stress in the silicon-doped Q-carbon structure. The de-strained bonds vibrate with lower frequencies. Thus, the downshift in the wavenumbers of the D and G peaks is partially related to the internal stress reduction. The addition of silicon to the structure also weakens the bonds between the C–C bonds by forming Si–C bonds and culminates in the downshift of the D and G peaks and the reduction in the intensity ratio of the peaks (I_D/I_G) [20–22,24]. The increase in the I_D/I_G ratio is proportional to the increase in the sp^2/sp^3 ratio [23,25–29]. The fitting results represent the I_D/I_G values of approximately 0.26, 0.23, and 0.20 for the samples with thicknesses of 35 nm, 20 nm, and 9 nm, respectively. Hence, the sp^3 content of the sample with a thickness of 9 nm is the highest, and the sp^3 content of the sample with a thickness of 35 nm is the lowest. The trend of the changes in sp^2 and sp^3 content with the changes in the thickness of Si-Q-carbon films will be further investigated to understand the basis of these changes. A typical Raman signal from silicon-doped diamond-like carbon structures is shown in the supplementary file (Fig. S.1). The results indicate the enhancement in the sp^3 content of the Si-Q-carbon structures in comparison with the silicon-doped diamond-like carbon structures.

To confirm and quantify the sp^3 and sp^2 carbon-carbon content of the three films, the room-temperature EELS close to the surface of the samples was carried out. The focused ion beam method was utilized to prepare the samples for EELS characterization. The enlarged spectra of the C–K edges of the three samples between 280 and 310 eV is illustrated in Fig. 2. The samples show the characteristic C–K edge EELS signal of Q-carbon structures. A typical EELS spectrum of Q-carbon consists of a π* peak with the onset of ~284 eV and a broad σ* peak with the onset of ~290 eV [30]. The π* peak is assigned to the sp^2-hybridized orbitals, and the σ* peak reveals the presence of the sp^3-hybridized atomic orbitals in the Q-carbon structure. When comparing the π* region of the three samples in Fig. 2, it is evident that the π* region in the sample with 35 nm thickness is greater than that of the other two samples; the thinnest sample (9 nm) has the smallest π* region. Therefore, qualitatively, the thinnest sample (9 nm) has the highest sp^3 content, and the 35 nm sample has the lowest sp^3 content.

To quantify the carbon-carbon sp^2 and sp^3 fraction of each sample, the C–K edges are fitted using the Gaussian fitting routine [31,32]. The sp^2 content can be estimated by comparing the π^*/σ^* value of the sample with a known π^*/σ^* using the following equation [33,34]:

$$\frac{(\pi^*/\sigma^*)_{carbon\ structure}}{(\pi^*/\sigma^*)_{std}} = \frac{3x}{4-x} \quad (1)$$

where x is the sp^2 fraction and $(\pi^*/\sigma^*)_{std}$ is equal to 1/3, which is the π^*/σ^* value for graphite. Graphite is utilized as the reference material since it is composed of 100% sp^2 bonds [35]. Fig. 3 depicts the Gaussian fitting of the C–K edges of the samples. The C–K edges can be fitted using the three characteristic peaks of C═C π*, C═C σ_1*, and C–C σ_2*. The sp^2 fractions estimated from Eq. (1) are ~14% ($sp^3 \approx 86\%$), ~23% ($sp^3 \approx 77\%$), and ~27% ($sp^3 \approx 73\%$) for the samples with a thickness of 9 nm, 20 nm, and 35 nm, respectively. Thus, the trend of changes in sp^3 content with changes in thickness is consistent with the results obtained from Raman analysis. The 9 nm silicon-doped Q-carbon sample contains

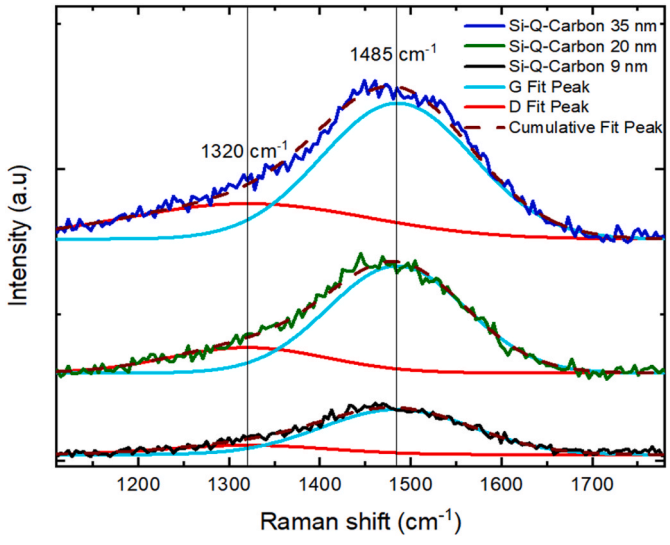

Fig. 1. The Raman spectra of the three samples with different thicknesses (Si-Q-carbon refers to the silicon-doped Q-carbon structure). (A colour version of this figure can be viewed online.)

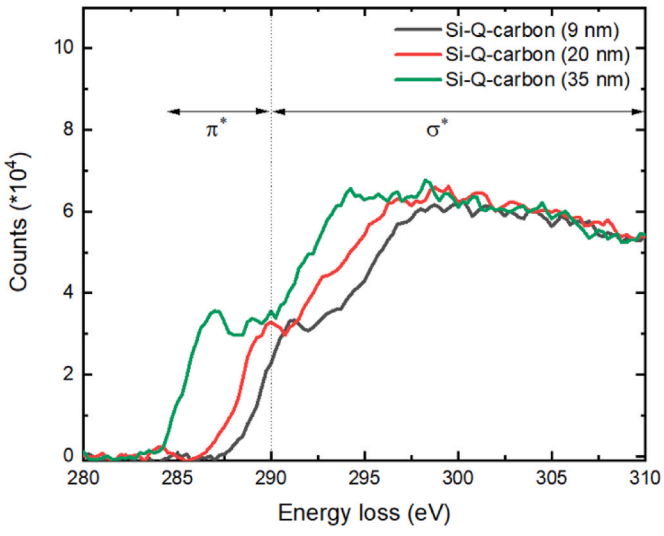

Fig. 2. The C–K edge EELS spectra of the three samples with different thicknesses. (A colour version of this figure can be viewed online.)

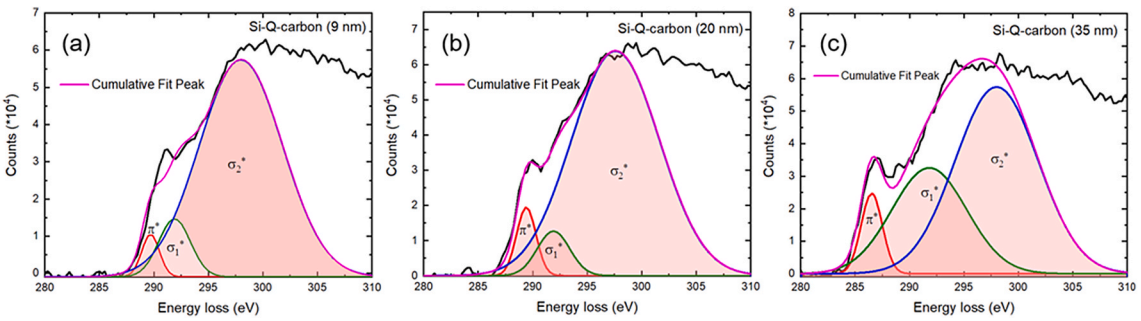

Fig. 3. The Gaussian fitting of the C–K edges of the samples with different thicknesses. (A colour version of this figure can be viewed online.)

approximately 86% sp^3 C–C bonds; in comparison, the typical value of sp^3 content for silicon-doped diamond-like carbon (Si-DLC) structures is ~55% [32]. Hence, low-energy ion bombardment has effectively promoted the formation of sp^3 bonds, prevented the formation of sp^2 bonds, and resulted in the generation of silicon-doped Q-carbon. The mechanisms of how the low-energy ion bombardment facilitates the generation of Si-Q-carbon will be discussed later.

The XPS analysis provides the bonding information and the elemental composition near the surface. Fig. 4(a) highlights the XPS spectra acquired from the three samples and shows the presence of silicon, carbon, and oxygen in the structures of all of the samples. Fig. 4(b) summarizes the atomic ratio (atomic%) of carbon, silicon, and oxygen that is present on the surface of the samples. From Fig. 4(b), it is clear that the atomic ratio of the Si-Q-carbon samples with 9 and 20 nm thickness are similar; the atomic ratios for these two samples are different from that of the 35 nm sample. On the surface of the 35 nm sample, the atomic percent of oxygen is significantly higher than the other two samples. The increase in the oxygen content on the surface of the 35 nm sample may occur due to the sputtering of the chamber walls with the ions from the low-energy ion bombardment process. The oxygen-containing bonds exist on the walls of the chamber from previous use of the chamber with oxygen gas or from moisture and provide the source of oxygen. Since the desorption of the oxygen-containing species from the walls of the chamber depends on time, by increasing the thickness of the samples with a longer deposition time, the contamination of the sample with oxygen is increased. As such, the 35 nm sample contains a higher amount of oxygen on its surface. We will further examine this matter with EDS characterization.

The XPS high-resolution C 1s spectra (Fig. 5) reveal the bonding characteristics of the samples. Fig. 5(a) shows that the C 1s band of the samples becomes broader and less conspicuous with increasing thickness. Thus, the sp^3 content of the samples is decreasing with increasing thickness. The tail of the spectra in the region of 286–290 eV becomes more dominant with increasing thickness, implying an increase in the oxygen-carbon bond content. The Shirley model was used for the background omission, and the Gaussian distribution model was applied following a previous approach [36] to appropriately establish the deconvoluted peaks. The deconvoluted bonds observed at 283.5, 284, 284.9, 286.4, and 288 eV are attributed to Si–C bonds, sp^2-hybridized carbon bonds, sp^3-hybridized carbon bonds, C–O bonds, and C═O bonds, respectively [37]. The 35 nm sample also shows the presence of O–C═O bonds at 289.5 eV. The content (%) of each bond is displayed in Table 1. Table 1 indicates that by increasing the thickness, the Si–C content and carbon-carbon sp^3 content decrease, while the carbon-carbon sp^2 content and oxygen-carbon content increase. The sp^3 content of the 9 nm sample was almost 80%; in comparison, our previous XPS sp^3 quantification results for the silicon-doped diamond-like carbon (Si-DLC) structure [32] that was produced using the same PECVD system without applying the low-energy ion bombardment was ~55%. The XPS data may indicate lower sp^3 content in comparison with the EELS data since the carbon-oxygen and carbon-silicon bonds are also considered in the XPS calculations. Hence, the results are in good agreement with the Raman and EELS data; in addition, the results predict the formation of oxygen-containing bonds on the surface over the time of deposition with increasing thickness.

The focused ion beam method was utilized to prepare samples for the

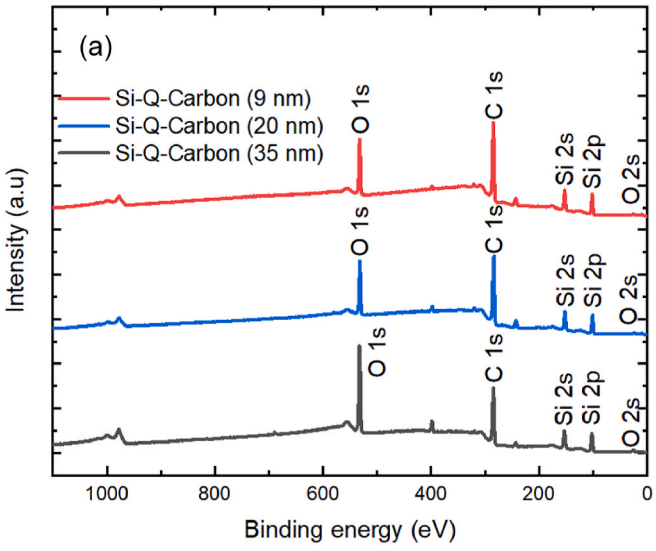

(b)

Si-Q-Carbon Sample	Peaks in XPS spectra		
	C 1s	Si 2p	O 1s
	Atomic (%)		
9 nm	65.4	15.43	17.69
20 nm	65.05	15.39	16.97
35 nm	49.31	15.59	28.58

Fig. 4. (a) The XPS spectra of the Si-Q-carbon samples, and (b) the atomic ratio of the elements (in atomic%) present on the surface of the samples. (A colour version of this figure can be viewed online.)

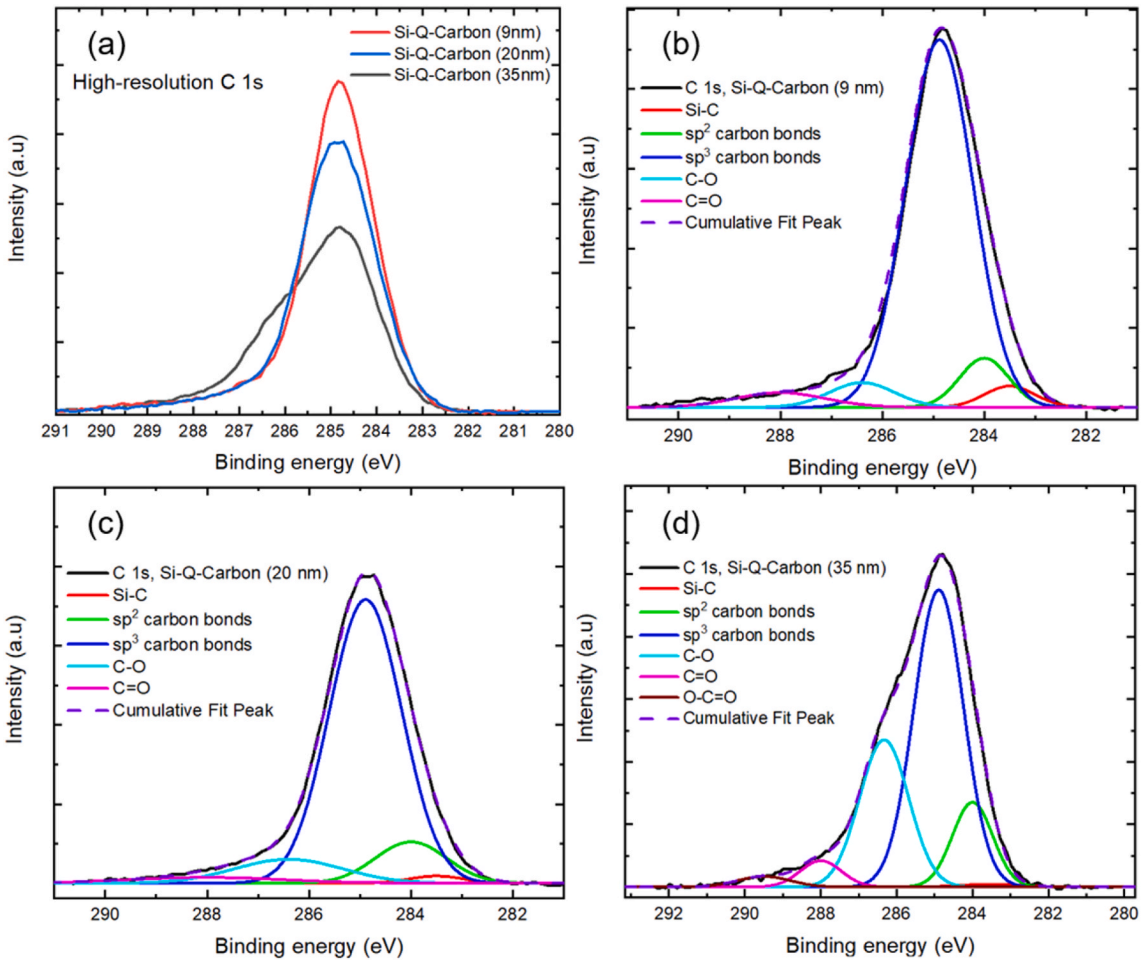

Fig. 5. (a) The high-resolution C 1s bands of the three samples, and the deconvolution of the high-resolution C 1s band of (b) 9 nm Si-Q-carbon, (c), 20 nm Si-Q-carbon, and (d) 35 nm Si-Q-carbon. (A colour version of this figure can be viewed online.)

Table 1
The content (%) of each bond from the deconvolution of the C 1s bands of the three samples.

Si-Q-carbon	Deconvoluted Peaks in C 1s spectra					
	Si–C	sp^2	sp^3	C–O	C=O	O–C=O
	Content (%)					
9 nm	3.4	7.7	79.6	5.1	4.2	–
20 nm	1.4	10.7	75.2	9.4	3.3	–
35 nm	0.6	12.54	54.21	26.6	3.99	2.06

high-resolution transmission electron microscopy imaging (Fig. 6(a–c)) and EDS mapping (Fig. 6(d–f)). The red rectangles in the figures show the position of the Si-Q-carbon films. The thickness values observed in Fig. 6(a–c) match the thickness values obtained from the contact profilometry method. In EDS mapping (Fig. 6(d–f)), the elements are marked with different colors: carbon in green color, oxygen in red color, and silicon in orange color. A layer of SiO_2 that normally exists on the surface of silicon substrates can be observed under the three Si-Q-carbon layers. The dominated color in the Si-Q-carbon layers is green, indicating the presence of carbon as the main element. In Fig. 6(f), an oxygen-rich layer can be observed on the top surface of the 35 nm Si-Q-carbon layer. This layer confirms the results obtained from XPS characterization and is the result of the time-dependent effusion of the oxygen from the chamber walls during the ion bombardment process.

3.2. The mechanism of Si-Q-carbon formation by low-energy ion bombardment

During the deposition step with argon and TMS gases, a negative bias of ~150 V was applied to the substrate, resulting in the bombardment of the substrate with a high dose of positive ions (on the order of 10^{15}-10^{17} cm^{-2} s^{-1} [10,13,38]). Generally, in the plasma of Ar/TMS, the main generated ions with intense signals characterized by mass spectrometry (MS) and optical emission spectroscopy (OES) are [39]: H_3^+, Ar^+, $C_3H_5^+$, ArH^+, CH_3^+, $SiCH^+$, $SiH_2CH_3^+$, $SiH(CH_3)_2^+$, and $Si(CH_3)_3^+$. Among them, CH_3^+ ions with an energy of 150 eV (bias voltage × charge) are not able to generate Frenkel pairs in the amorphous carbon structure upon collision to the surface. The Number of the Frenkel pairs (N_{FP}), which are vacancy-interstitial pairs, can be estimated using [40]:

$$N_{FP} = \frac{0.8E_D}{2E_d} \tag{2}$$

where E_d is the threshold energy of damage and E_D is the damage energy that can be calculated for low-energy ions by:

$$E_D = \frac{4m_1m_2E_i}{(m_1+m_2)^2} \tag{3}$$

where m_1, m_2, and E_i are the mass of the incident ion, the mass of substrate, and incident ion energy, respectively. Considering the threshold damage energy or the displacement energy of diamond (E_d) as 45–70 eV [41,42], the CH_3^+ ions with 150 eV energy are not able to create Frenkel pairs upon bombarding the surface of amorphous carbon

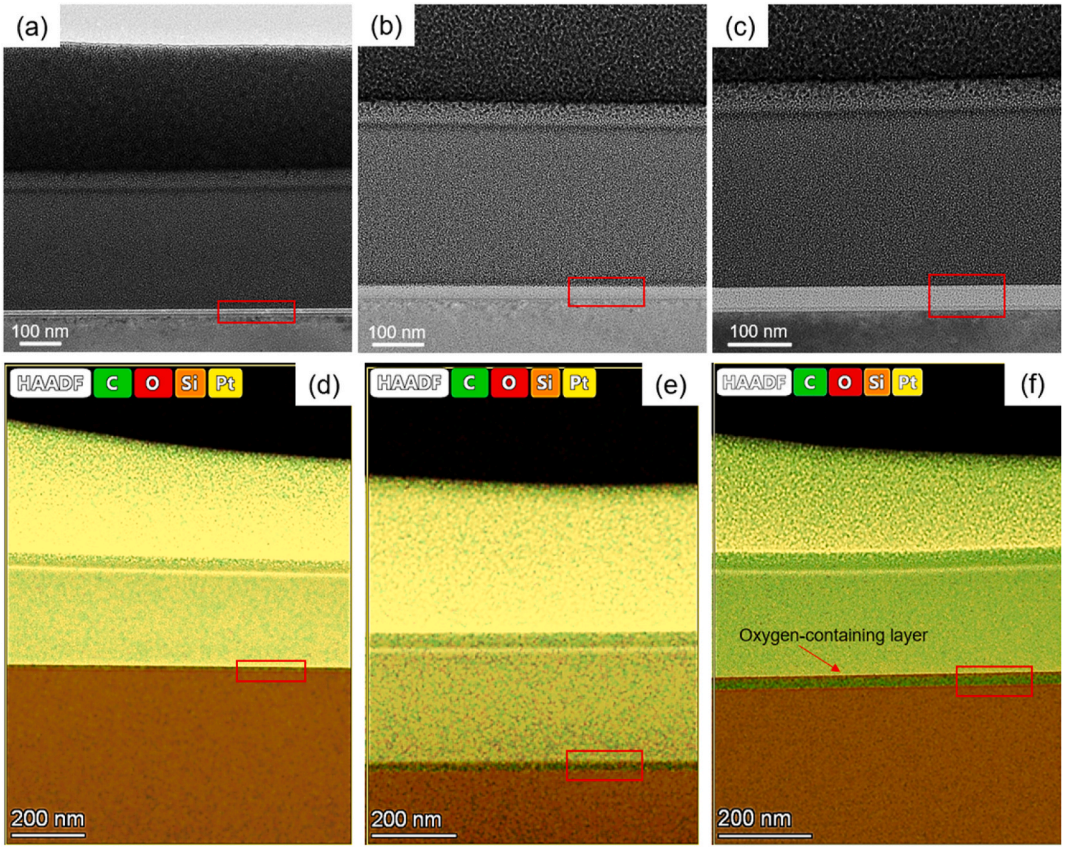

Fig. 6. The high-resolution transmission electron microscopy of the samples with a thickness of: (a) 9 nm, (b) 20 nm, and (c) 35 nm. The EDS map of the samples with a thickness of: (d) 9 nm, (e) 20 nm, and (f) 35 nm. (A colour version of this figure can be viewed online.)

(assuming $E_d = 70$ eV). Thus three-fold coordinated carbons are not converted into the tetrahedron units with a central atom (consisting of five four-fold coordinated carbons) [6].

To promote the generation of Frenkel pairs and the conversion of sp^2-bonded carbons into sp^3-bonded carbons, postprocessing of surface treatment on the samples was performed utilizing argon plasma. During this process, the surface of the samples was bombarded using argon plasma with a negative bias of ~250 V. The argon ions with an energy of ~250 eV are able to generate one Frenkel pair per each argon ion. Considering the high dose of argon ions of up to 10^{17} cm^{-2} s^{-1}, the argon surface treatment can effectively convert ~10 nm thick amorphous carbon structure into the Q-carbon phase. This Q-carbon conversion for thicker layers beyond 10 nm is only partial. It is noteworthy to consider that the energy of argon ions is not sufficiently high to generate significant damage to the structure and prohibit the formation of sp^3 carbon bonds. We estimate that multiple Frenkel pairs produced by Ar^+ ions in the energy range of 500 eV–1000 eV may lead to more damage and thus not be conducive to the formation of Q-carbon.

4. Conclusions

Low-energy ion bombardment through applying negative bias was utilized during the PECVD deposition to transform the low sp^3-content amorphous carbon structure into a Q-carbon structure. Ar and TMS were used as the processing gases for the deposition of Si-Q-carbon. For further transformation of the three-fold coordinated carbons into five-atom tetrahedron units, postprocessing of the samples using Ar^+ ion bombardment with a ~250 eV negative bias was carried out. The EELS, XPS, and Raman analyses confirm that the energy of the CH_3^+ ions during the deposition and the energy of the Ar^+ ions during the postprocessing were adequate for this transformation into Si-doped Q-carbon structure with a sp^3 carbon content of up to 86% was formed on a 6" silicon wafer. With the low-energy ion bombardment method, we deposited three different thicknesses of Si-Q-carbon (9 nm, 20 nm, and 35 nm). The 250 eV Ar^+ ion bombardment is able to convert ~10 thick amorphous carbon into Q-carbon effectively. For thicker carbon layers this conversion into Q-carbon was only partial. Applying ion bombardment with an optimized energy is important for the successful generation of the Q-carbon phase. The energy of the ions during low-energy ion bombardment should be high enough to contribute to the formation of Frenkel pairs and the generation of five-atom tetrahedron units. However, with a further increase in the energy of the ions during ion bombardment, the stress induced by the ions is much higher and faster than the relaxation time (the time for the transformation of sp^2 bonds into sp^3 bonds); this phenomenon causes graphitization and an increase in the sp^2 content. Since Q-carbon can be converted readily into nanodiamonds with additional laser pulses, these Si-doped Q-carbon layers provide an ideal platform to create SiV nanodiamonds for nanosensing and qubits for quantum computing. Our recent results on magnetic measurements have shown robust ferromagnetism at room temperature in Si-doped Q-carbon. The coercivity and saturation magnetization decrease with increasing thickness. This finding is consistent with a decreasing fraction of Q-carbon. The details of this work will be reported shortly [43].

CRediT authorship contribution statement

Parand R. Riley: Methodology, experimental work, Formal analysis, Data curation, and interpretation of the data. **Pratik Joshi:** Formal analysis, Data curation, and interpretation of the data. **Nayna Khosla:** Formal analysis, Data curation, and interpretation of the data. **Roger J. Narayan:** Conceptualization, Funding acquisition, Data curation, and interpretation of the data. **Jagdish Narayan:** Conceptualization,

Funding acquisition, Data curation, and interpreting the data.

Declaration of competing interest

The authors declare that they have no known competing financial interests or personal relationships that could have appeared to influence the work reported in this paper.

Acknowledgments

The authors would like to acknowledge the support of National Science Foundation Awards #1836767 and #2016256.

Appendix A. Supplementary data

Supplementary data to this article can be found online at https://doi.org/10.1016/j.carbon.2022.06.003.

References

[1] J. Narayan, A. Bhaumik, Novel phase of carbon, ferromagnetism, and conversion into diamond, J. Appl. Phys. 118 (21) (2015), 215303, https://doi.org/10.1063/1.4936595. US Patents: 10586702 & 105666193.
[2] J. Narayan, S. Gupta, A. Bhaumik, R. Sachan, F. Cellini, E. Riedo, Q-carbon harder than diamond, MRS Communications 8 (2) (2018) 428–436, https://doi.org/10.1557/mrc.2018.35.
[3] J. Narayan, A. Bhaumik, R. Sachan, High temperature superconductivity in distinct phases of amorphous B-doped Q-carbon, J. Appl. Phys. 123 (2018), 135304, https://doi.org/10.1063/1.5016397.
[4] J. Narayan, A. Bhaumik, S. Gupta, A. Haque, R. Sachan, Progress in Q-carbon and related materials with extraordinary properties, Mater. Res. Lett. 6 (2018) 353–364, https://doi.org/10.1080/21663831.2018.1458753.
[5] A. Bhaumik, R. Sachan, S. Gupta, J. Narayan, Discovery of high-temperature superconductivity (T c = 55 K) in B-doped Q-carbon, ACS Nano 11 (2017) 11915–11922, https://doi.org/10.1021/acsnano.7b06888.
[6] J. Narayan, A. Bhaumik, S. Gupta, P. Joshi, P. Riley, R.J. Narayan, Role of Q-carbon in nucleation and formation of continuous diamond film, Carbon 196 (2021) 558–568, https://doi.org/10.1016/j.carbon.2021.02.049.
[7] J. Narayan, N. Khosla, Self-organization of amorphous Q-carbon and Q-BN nanoballs, Carbon 192 (2022) 301–307, https://doi.org/10.1016/j.carbon.2022.03.003.
[8] R. Sachan, S. Gupta, J. Narayan, Nonequilibrium structural evolution of Q-carbon and interfaces, ACS Appl. Mater. Interfaces 12 (2020) 1330–1338, https://doi.org/10.1021/acsami.9b17428.
[9] S. Yugo, T. Kanai, T. Kimura, T. Muto, Generation of diamond nuclei by electric field in plasma chemical vapor deposition, Appl. Phys. Lett. 58 (1991) 1036–1038, https://doi.org/10.1063/1.104415.
[10] B.R. Stoner, G.H.M. Ma, S.D. Wolter, J.T. Glass, Characterization of bias-enhanced nucleation of diamond on silicon by invacuo surface analysis and transmission electron microscopy, Phys. Rev. B 45 (1992) 11067–11084, https://doi.org/10.1103/PhysRevB.45.11067.
[11] Y.K. Kim, Y.S. Han, J.Y. Lee, The effects of a negative bias on the nucleation of oriented diamond on Si, Diam. Relat. Mater. 7 (1998) 96–105, https://doi.org/10.1016/S0925-9635(97)00195-7.
[12] M. Schreck, T. Bauer, S. Gsell, F. Hörmann, H. Bielefeldt, B. Stritzker, Domain formation in diamond nucleation on iridium, Diam. Relat. Mater. 12 (2003) 262–267, https://doi.org/10.1016/S0925-9635(02)00361-8.
[13] M. Liao, F. Qin, J. Zhang, Z. Liu, S. Yang, Z. Wang, S.T. Lee, Ion bombardment as the initial stage of diamond film growth, J. Appl. Phys. 89 (2001) 1983–1985, https://doi.org/10.1063/1.1338997.
[14] M. Schreck, S. Gsell, R. Brescia, M. Fischer, Ion bombardment induced buried lateral growth: the key mechanism for the synthesis of single crystal diamond wafers, Sci. Rep. 7 (2017), https://doi.org/10.1038/srep44462.
[15] Y. Lifshitz, T. Köhler, T. Frauenheim, I. Guzmann, A. Hoffman, R.Q. Zhang, X. T. Zhou, S.T. Lee, The mechanism of diamond nucleation from energetic species, Science (80 297 (2002) 1531–1533, https://doi.org/10.1126/science.1074551.
[16] A. Dychalska, P. Popielarski, W. Frankow, K. Fabisiak, K. Paprocki, M. Szybowicz, Study of CVD diamond layers with amorphous carbon admixture by Raman scattering spectroscopy, Sciendo.Com. 33 (2015) 799–805, https://doi.org/10.1515/msp-2015-0067.
[17] A. Meščeriakovas, Synthesis, characteristics and application of doped carbon structures. https://erepo.uef.fi/bitstream/handle/123456789/25226/urn_isbn_978-952-61-3809-1.pdf, 2021. (Accessed 14 February 2022).
[18] P.R. Riley, P. Joshi, H. Penchev, J. Narayan, R.J. Narayan, One-step formation of reduced graphene oxide from insulating polymers induced by laser writing method, Crystals 11 (2021) 1308, https://doi.org/10.3390/cryst11111308.
[19] P. Joshi, P.R. Riley, W. Denning, S. Shukla, N. Khosla, J. Narayan, R. Narayan, Laser-patterned carbon coatings on flexible and optically transparent plastic substrates for advanced biomedical sensing and implant applications, J. Mater. Chem. C. 10 (2022) 2965–2975, https://doi.org/10.1039/d1tc05176h.
[20] Š. Meškinis, A. Vasiliauskas, M. Andrulevičius1, D. Peckus, S. Tamulevičius, K. Viskontas, Diamond like carbon films containing Si: structure and nonlinear optical properties, Materials (Basel) 13 (2020) 1003, https://doi.org/10.3390/ma13041003.
[21] J. Wang, G. Liu, J. Xu, X. Deng, L. Wang, Nanomechanical and electrochemical properties of diamond-like carbon (DLC) films deposited by plasma enhanced chemical vapor deposition (PECVD) technique, Plasma Sci. Technol. 12 (2010) 461–465, https://doi.org/10.1088/1009-0630/12/4/15.
[22] C.T. Guo, Diamond-like carbon films deposited on polycarbonates by plasma-enhanced chemical vapor deposition, Thin Solid Films 516 (2008) 4053–4058, https://doi.org/10.1016/j.tsf.2008.01.010.
[23] F. Zhao, H.X. Li, L. Ji, Y.F. Mo, W.L. Quan, H.D. Zhou, J.M. Chen, Structural, mechanical and tribological characterizations of a-C : HH : SSi films prepared by a hybrid PECVD and sputtering technique, J. Phys. D Appl. Phys. 42 (2009), 165407, https://doi.org/10.1088/0022-3727/42/16/165407.
[24] X.M. He, K.C. Walter, M. Nastasi, S.-T. Lee, M.K. Fung, Investigation of Si-doped diamond-like carbon films synthesized by plasma immersion ion processing, J. Vac. Sci. Technol. A Vacuum, Surfaces, Film. 18 (2000) 2143, https://doi.org/10.1116/1.1286141.
[25] N. Shimodaira, A. Masui, Raman spectroscopic investigations of activated carbon materials, J. Appl. Phys. 92 (2002) 902, https://doi.org/10.1063/1.1487434.
[26] F.C. Tai, S.C. Lee, C.H. Wei, S.L. Tyan, Correlation between ID⁄IG ratio from visible Raman spectra and sp2/sp3 ratio from XPS spectra of annealed hydrogenated DLC film, Jstage.Jst.Go.Jp. (n.d.). https://doi.org/10.2320/matertrans.47.1847.
[27] G. Irmer, A. Dorner-Reisel, Micro-Raman studies on DLC coatings, Adv. Eng. Mater. 7 (2005) 694–705, https://doi.org/10.1002/adem.200500006.
[28] A. Ferrari, J. Robertson, Interpretation of Raman spectra of disordered and amorphous carbon, Phys. Rev. B Condens. Matter 61 (2000) 14095–14107, https://doi.org/10.1103/PhysRevB.61.14095.
[29] A.C. Ferrari, S.E. Rodil, J. Robertson, W.I. Milne, Is stress necessary to stabilise sp3 bonding in diamond-like carbon? Diam. Relat. Mater. 11 (2002) 994–999, https://doi.org/10.1016/S0925-9635(01)00705-1.
[30] S. Gupta, R. Sachan, A. Bhaumik, J. Narayan, Enhanced mechanical properties of Q-carbon nanocomposites by nanosecond pulsed laser annealing, Nanotechnology 29 (2018), https://doi.org/10.1088/1361-6528/aadd75.
[31] D. Galvan, Y.T. Pei, J.T.M. De Hosson, A. Cavaleiro, Determination of the sp3 C content of a-C films through EELS analysis in the TEM, Surf. Coating. Technol. 200 (2005) 739–743, https://doi.org/10.1016/j.surfcoat.2005.02.071.
[32] P.R. Riley, P. Joshi, S.A. Machekposhti, R. Sachan, J. Narayan, R.J. Narayan, Enhanced vapor transmission barrier properties via silicon-incorporated diamond-like carbon coating, Polymers 13 (2021) 3543, https://doi.org/10.3390/polym13203543.
[33] J.J. Cuomo, J.P. Doyle, J. Bruley, J.C. Liu, Sputter deposition of dense diamond-like carbon films at low temperature, Appl. Phys. Lett. 58 (1991) 466–468, https://doi.org/10.1063/1.104609.
[34] J. Bruley, D.B. Williams, J.J. Cuomo, D.P. Pappas, Quantitative near-edge structure analysis of diamond-like carbon in the electron microscope using a two-window method, J. Microsc. 180 (1995) 22–32, https://doi.org/10.1111/j.1365-2818.1995.tb03653.x.
[35] H. Daniels, R. Brydson, B. Rand, A. Brown, Investigating carbonization and graphitization using electron energy loss spectroscopy (EELS) in the transmission electron microscope (TEM), Philos. Mag. A 87 (2007) 4073–4092, https://doi.org/10.1080/14786430701394041.
[36] C. Önneby, C.G. Pantano, Silicon oxycarbide formation on SiC surfaces and at the SiC/SiO2 interface, J. Vac. Sci. Technol. 15 (1997) 1597–1602, https://doi.org/10.1116/1.580951.
[37] P.R. Riley, P. Joshi, J. Narayan, R.J. Narayan, Enhanced nucleation and large-scale growth of CVD diamond via surface-modification of silicon-incorporated diamond-like carbon thin films, Diam. Relat. Mater. 120 (2021), 108630, https://doi.org/10.1016/j.diamond.2021.108630.
[38] S. Kátai, A. Kováts, I. Maros, P. Deák, Ion energy distributions and their evolution during bias-enhanced nucleation of chemical vapor deposition of diamond, Diam. Relat. Mater. 9 (2000) 317–321, https://doi.org/10.1016/S0925-9635(99)00216-2.
[39] Á. Yanguas-Gil, Á. Barranco, J. Cotrino, P. Gröning, A.R. Gonzalez-Elipe, Plasma characterization of oxygen-tetramethylsilane mixtures for the plasma-enhanced CVD of SiOxCyHz thin films, Chem. Vap. Depos. 12 (2006) 728–735, https://doi.org/10.1002/cvde.200606496.
[40] J. Narayan, O.W. Holland, Characteristics of ion-implantation damage and annealing phenomena in semiconductors, J. Electrochem. Soc. 131 (1984) 2651–2662, https://doi.org/10.1149/1.2115377.
[41] W.M. Lau, L.J. Huang, I. Bello, Y.M. Yiu, S.T. Lee, Modification of surface band bending of diamond by low energy argon and carbon ion bombardment, J. Appl. Phys. 75 (1994) 3385–3391, https://doi.org/10.1063/1.357016.
[42] J. Koike, D.M. Parkin, T.E. Mitchell, Displacement threshold energy for type IIa diamond, Appl. Phys. Lett. 60 (1992) 1450–1452, https://doi.org/10.1063/1.107267.
[43] N. Joshi, P. Riley, R. Narayan, and J. Narayan, (Manscript to be Published).